Materials Advances

ROYAL SOCIETY OF CHEMISTRY

PAPER

View Article Online
View Journal | View Issue

Cite this: *Mater. Adv.*, 2025, **6**, 7585

Nanoflower-like ZnO–carbon quantum dot heterostructures for solar-driven degradation of methylene blue: a high-performance and recyclable photocatalyst for sustainable wastewater treatment

Hitesh Bansal,† Palkaran Sethi† and Soumen Basu *

Developing robust, high-performance photocatalysts for environmental remediation remains a critical scientific pursuit. This work successfully synthesized novel ZnO–carbon quantum dot (CQD) heterostructured nanocomposites with distinct nanoflower-like morphology by incorporating 5%, 10%, and 15% CQDs onto ZnO surfaces. The strategic integration of CQDs not only enhanced solar light harvesting and facilitated superior charge carrier separation, but also improved the recyclability and stability of the composites, surpassing the limitations of conventional photocatalytic systems. Comprehensive characterization using XRD, FTIR, XPS, BET, PL, UV-Vis-DRS, FE-SEM, EDS, and HR-TEM analyses confirmed the synthesized composites' high crystallinity, enlarged surface area, morphology, and light response. Photocatalytic studies conducted under natural sunlight irradiation demonstrated an impressive 97.7% degradation of methylene blue (MB) in merely 60 minutes, following pseudo-first-order kinetics and achieving a rate constant of about 0.047 min^{-1}, which is 5.7 times greater than that of the benchmark TiO_2–P25 catalyst. Systematic investigations of solution pH, photocatalyst dosage, light sources, and radical scavenging further validated the robustness and versatility of the composite. Impressively, the ZnO/CQD nanocomposite retained 85% of its photocatalytic efficiency after six consecutive cycles, demonstrating exceptional reusability and operational stability. The photocatalytic degradation pathway was determined using LC-MS analysis, showing notable decreases of 65% in TOC (total organic carbon) and 58% in COD (chemical oxygen demand), which confirmed effective mineralization. Given the persistence, toxicity, and carcinogenic potential of MB in aquatic ecosystems, this study introduces a sustainable, scalable, and highly effective solar-driven photocatalyst. These outstanding results position the ZnO/CQD nanocomposite as a leading candidate for next-generation wastewater remediation technologies and offer a compelling advancement warranting publication in high-impact scientific forums.

Received 24th July 2025,
Accepted 13th September 2025

DOI: 10.1039/d5ma00804b

rsc.li/materials-advances

1. Introduction

The rapid growth of global urban populations has significantly escalated the demand for clean water, resulting in critical shortages and emphasizing the urgent need to address water scarcity challenges.[1] This crisis is further intensified by the increasing contamination of freshwater resources with industrial pollutants, including synthetic dyes, heavy metals, and persistent organic compounds.[2] Among these, synthetic dyes pose a serious environmental threat due to their structural complexity, resistance to degradation, and toxicity.[3] Extensively used in textiles, printing, leather, cosmetics, pharmaceuticals, and food industries,[4] these dyes can severely impact aquatic ecosystems and human health even at low concentrations.

Methylene blue (MB), a widely used cationic dye in medical and industrial applications, is known for its carcinogenicity, mutagenicity, and persistence in water bodies.[5–7] Its removal from wastewater is imperative, yet conventional treatment methods—including biological processes,[8] chemical oxidation,[9] adsorption,[10] photocatalysis,[11] and membrane-based physical separation[12]—often fall short due to high cost, incomplete degradation, and secondary pollution. Photocatalysis, as a form of the advanced oxidation process (AOP), has emerged as a promising alternative due to its ability to completely mineralize organic contaminants

Department of Chemistry and Biochemistry, Thapar Institute of Engineering & Technology, Patiala-147004, India. E-mail: soumen.basu@thapar.edu
† Both authors have contributed equally.

under mild conditions.[13] This technique involves the generation of reactive oxygen species (ROS) through light-activated semiconductors, which oxidize and break down complex organic molecules.

Several semiconductor materials—such as TiO_2, Fe_2O_3, CdS, ZnS, GaP, and P_2Mo_{18}—have been extensively investigated for photocatalytic applications.[14–16] Among them, ZnO has garnered significant attention due to its high electron mobility, strong oxidizing potential, low cost, chemical stability, and environmental compatibility.[17–19] Despite these advantages, ZnO suffers from a wide band gap ($\sim$3.2 eV), which restricts its activity to the UV region, and rapid recombination of photoinduced charge carriers, both of which limit its overall photocatalytic efficiency.[20]

To overcome these limitations, various strategies have been employed, including element doping, surface modification, and formation of heterojunctions. As a new class of carbon nanomaterials, carbon quantum dots (CQDs), which exhibit fluorescence, have also gained attention as co-catalysts in photocatalysis due to their broad visible light absorption, high photostability, upconversion photoluminescence and excellent electron transfer properties.[21] When composited with ZnO, CQDs can significantly enhance visible light responsiveness, improve charge separation, and promote photocatalytic activity. The synergistic interaction between ZnO and CQDs results in efficient suppression of electron–hole recombination and facilitates prolonged charge carrier lifetimes.[22]

Several CQD-modified ZnO systems have been studied for organic pollutant degradation. For example, lanthanum-doped ZnO nanotubes showed effective MB degradation under sunlight at pH 9 within 90 min.[23] Also, sulfur-doped ZnO films degraded rhodamine B in 150 min under visible light with H_2O_2 assistance.[24] In another study, GO/ZnO composites doped with Ag or Au exhibited improved photocatalytic degradation of MB, although performance varied with metal dopants.[25] Nitrogen-doped CQDs from biomass demonstrated effective Malachite Green degradation under sunlight,[26] and ZnO/N,S-CQDs were used for ciprofloxacin removal under simulated light but showed reduced activity in real water samples.[27] However, most of these systems still face issues such as slow kinetics, limited reusability, narrow pH ranges, or incomplete mineralization—factors that restrict their practical applications.

To address these challenges, we developed a novel ZnO/CQD heterostructured nanocomposite with a flower-like ZnO morphology and varying CQD loadings (5%, 10%, and 15% by weight). The nanoflower morphology of ZnO provides a significant surface area and numerous active sites, whereas the CQDs improve visible light absorption and facilitate interfacial charge transfer. Its structural and optical properties were extensively characterized using XRD, XPS, FTIR, BET, PL, UV-vis DRS, FE-SEM, EDS, and HR-TEM. The photocatalytic performance was evaluated for MB degradation under natural sunlight, with investigations into catalyst dosage, pH, light source, degradation kinetics, and scavenger effects. LC-MS analysis was used to elucidate degradation intermediates, while TOC and COD measurements confirmed mineralization. The optimized ZnO/CQD composite showed rapid degradation, high reusability, and excellent solar-light-driven performance, addressing the critical limitations of prior systems and offering a scalable, sustainable solution for wastewater treatment.

2. Materials and reagents

2.1. Materials

Zinc nitrate hexahydrate ($Zn(NO_3)_2{\cdot}6H_2O$) (98% AR), L-ascorbic acid (99% extra pure), sodium hydroxide (NaOH) (97% extra pure), and methylene blue powder were obtained from Loba Chemie. The solutions were prepared using ultrapure double-distilled water. Pure reagents were used without any further purification.

2.2. Synthesis of zinc oxide nanoflowers

Zinc oxide (ZnO) nanoflowers were synthesized *via* a hydrothermal approach using $Zn(NO_3)_2{\cdot}6H_2O$ as the precursor. Briefly, 4.46 g of $Zn(NO_3)_2{\cdot}6H_2O$ was dissolved in 30 mL of deionized water under continuous magnetic agitation for 30 minutes to ensure complete dissolution. The solution's pH was adjusted to 12 by the dropwise addition of 5 M sodium hydroxide (NaOH) solution under constant stirring. The obtained homogeneous mixture was placed in a 100 mL Teflon-lined stainless-steel autoclave and subjected to heating at 125 °C for 2 hours in a muffle furnace, adhering to a previously documented procedure.[28] Following natural cooling to room temperature, the precipitate was collected through centrifugation at 6000 rpm for 4 minutes. It was then thoroughly washed with deionized water and ethanol multiple times to eliminate unreacted species, and finally dried at ambient temperature. The obtained white powder was designated as ZnO (Z) for further use.

2.3. Synthesis of CQDs

Carbon quantum dots (CQDs) were synthesized through a hydrothermal method using L-ascorbic acid as a carbon source. In this procedure, 2.0 g of L-ascorbic acid was carefully dissolved in 20 mL of deionized water while being subjected to magnetic stirring. The resulting clear solution was placed in a 50 mL Teflon-lined stainless-steel autoclave and subjected to heating at 180 °C for 8 hours in a muffle furnace, following the previously published procedure.[29] A light-yellow suspension was obtained after the completion of the reaction. The suspension was filtered through standard filter paper, and the resulting light brown filtrate—containing the CQDs—was collected. The solid residue remaining on the filter paper was discarded. The obtained CQD solution was labeled as Q for subsequent composite synthesis.

2.4. Synthesis of ZnO/CQD composites

To synthesize the ZnO/CQD nanocomposites, 950 mg of ZnO was carefully dispersed in a beaker containing 10 mL of the CQD solution. The solution was agitated for an extended period under ambient conditions to promote consistent interaction between ZnO and CQDs. After stirring, the suspension underwent centrifugation, and the resulting precipitate was meticulously

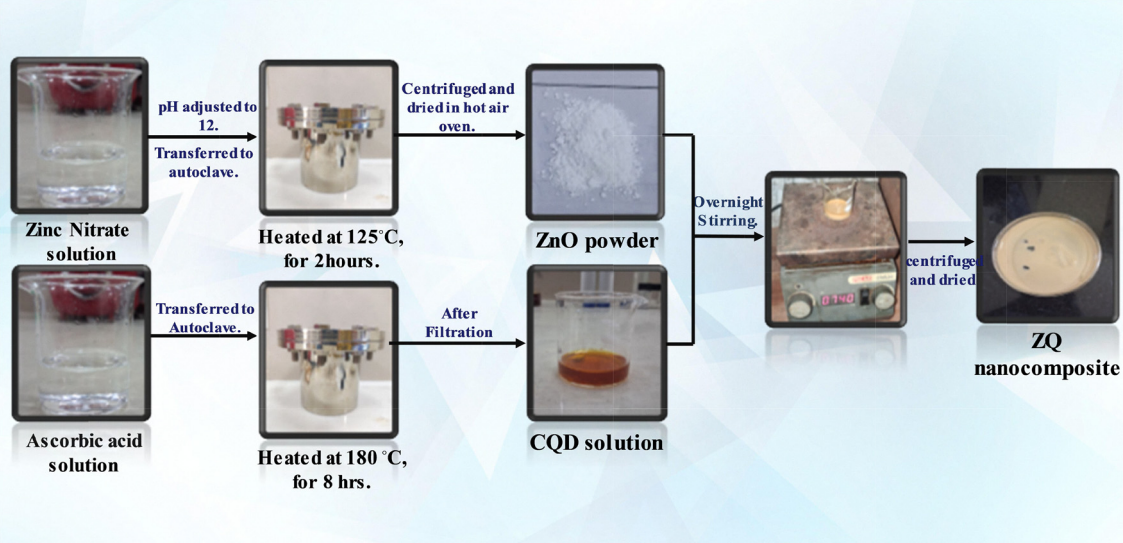

Scheme 1 Synthesis scheme of the ZnO/CQD nanocomposite.

washed with deionized water and ethanol to eliminate any residual impurities. The washed samples were subsequently dried overnight in a hot air oven. The obtained composite was designated as ZQ5, reflecting its CQD content. Similarly, other nanocomposites, namely ZQ10 and ZQ15, were prepared by varying the volume of CQD solution while keeping the ZnO weight constant, corresponding to 10% and 15% CQD loadings, respectively (Scheme 1).

3. Results and discussion

3.1. Characterization methods

A comprehensive array of analytical methods was utilized to characterize the structural, morphological, optical, and compositional attributes of the synthesized nanocomposites. The UV-visible absorption spectra were obtained using a Shimadzu UV-2600 spectrophotometer, and the photoluminescence (PL) spectra were measured using a Shimadzu RF-6000 spectrofluorometer. The surface morphology and particle dimensions were analyzed using field emission scanning electron microscopy (FE-SEM, JEOL), while the internal structure at the nanoscale was further explored through high-resolution transmission electron microscopy (HR-TEM, JEOL JEM-2100 Plus). X-ray diffraction (XRD) was employed for the identification of crystallinity and the structural analysis. The materials' functional groups were characterized by Fourier-transform infrared (FTIR) spectroscopy using a Shimadzu IRTracer-100. Diffuse reflectance UV-vis spectroscopy (UV-DRS) was conducted to evaluate the optical band gap characteristics. The specific surface area and pore size distribution were determined from nitrogen adsorption–desorption isotherms employing the Brunauer–Emmett–Teller (BET) and Barrett–Joyner–Halenda (BJH) methods with a Belsorp Mini II analyzer. The elemental composition and chemical bonding states were examined through X-ray photoelectron spectroscopy (XPS) utilizing a Versa Probe III system. Liquid chromatography-mass spectrometry (LC-MS) was conducted using a Waters Micromass Q-Tof micro instrument to identify degradation intermediates and clarify the mechanism of photocatalytic degradation. Analyses of total organic carbon (TOC) and chemical oxygen demand (COD) were conducted to determine the extent of mineralization of the dye and evaluate the effectiveness of the photocatalytic process.

3.1.1. XPS analysis. Fig. 1 presents the XPS analysis of the ZQ5 composite. As shown in Fig. 1(a), the survey spectrum confirms the presence of zinc (Zn), oxygen (O), and carbon (C) elements in the material. In Fig. 1(c), the Zn 2p spectrum exhibits two prominent peaks at binding energies of 1044.42 eV and 1021.30 eV, which correspond to Zn $2p_{1/2}$ and Zn $2p_{3/2}$, respectively.

The high-resolution O 1s spectrum of the composite displays two distinct peaks at 530.34 eV and 531.81 eV, which are associated with Zn–O and C–O bonds, respectively. These changes, in combination with FTIR results, suggest that the carboxyl groups from CQDs react with the surface hydroxyl groups on ZnO. This interaction probably results in a decrease or the elimination of hydroxyl signals and the creation of new C–O bonds, as illustrated in Fig. 1(b).

Additionally, the C 1s spectrum (Fig. 1(d)) of the CQD/ZnO composite features a peak at 284.21 eV, linked to C–C bonds in CQDs. Peaks at 285.78 eV and 288.55 eV are associated with C–O and C═C bonds, respectively. These spectral features confirm that CQDs have been successfully incorporated into the ZnO structure, forming a well-integrated composite.[30]

3.1.2. X-Ray diffraction. The crystallinity of the synthesized materials was examined using X-ray diffraction (XRD). The XRD patterns of ZnO, CQDs, and the nanocomposites (ZQ5, ZQ10, and ZQ15) are shown in Fig. 2(a). The diffraction pattern of ZnO exhibited characteristic peaks at 2θ values of 31.73°, 34.50°, 36.22°, 47.50°, 56.90°, and 62.85°, which are indexed to the (100), (002), (101), (102), (110), and (103) planes of hexagonal wurtzite ZnO, in agreement with JCPDS card no. 36-1451.[28]

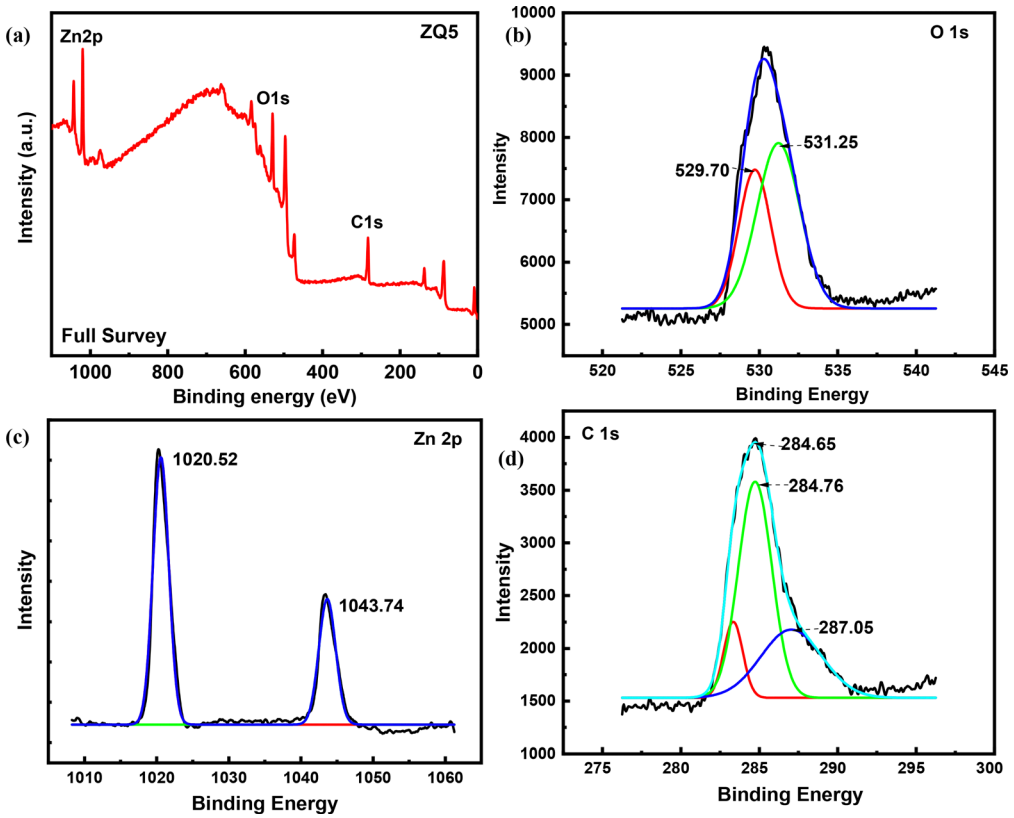

Fig. 1 (a) XPS full spectrum of ZQ5, (b) spectrum of O 1s, (c) spectrum of Zn 2p, and (d) spectrum of C 1s.

These sharp and well-defined peaks confirmed its high crystallinity and phase purity. In contrast, CQDs showed a broad diffraction peak centered around $2\theta \approx 21.02^{\circ}$, consistent with the amorphous carbon phase reported in previous studies.[29] Upon compositing, the diffraction patterns of the ZQ5, ZQ10, and ZQ15 samples retained the characteristic peaks of ZnO with little significant shift in peak positions, suggesting that the crystalline framework of ZnO was preserved. No distinct diffraction peaks corresponding to CQDs were observed in the composites, which may be attributed to their low content and predominantly amorphous nature.[31] These results indicate that the incorporation of CQDs did not alter the crystal structure of ZnO, but rather formed a surface-bound heterojunction.

3.1.3. Fourier transform infrared spectroscopy. FTIR spectroscopy was utilized to investigate the surface functionalities and chemical bonding of the pristine materials and their composites. Spectra were recorded across the range of 4000–400 cm^{-1}, as illustrated in Fig. 2(b). The spectrum of ZnO displayed a broad band near 3475 cm^{-1}, which corresponds to O–H stretching vibrations, typically arising from adsorbed water or hydroxyl groups. A peak at 2962 cm^{-1} was linked to C–H stretching, whereas the feature at 1633 cm^{-1} suggested C═O stretching associated with carbonyl groups. The bending vibrations of interstitial water molecules were evident at 752 cm^{-1}, alongside a deformation band near 644 cm^{-1}. Additionally, vibrational signatures associated with carbonate ions (CO_3^{2-}) were identified at 1507, 1382, and 845 cm^{-1}. A peak at 1560 cm^{-1} further confirmed the presence of symmetric C═O stretching vibrations.[28] CQDs exhibited a broad absorption region between 3135 and 3576 cm^{-1}, characteristic of O–H

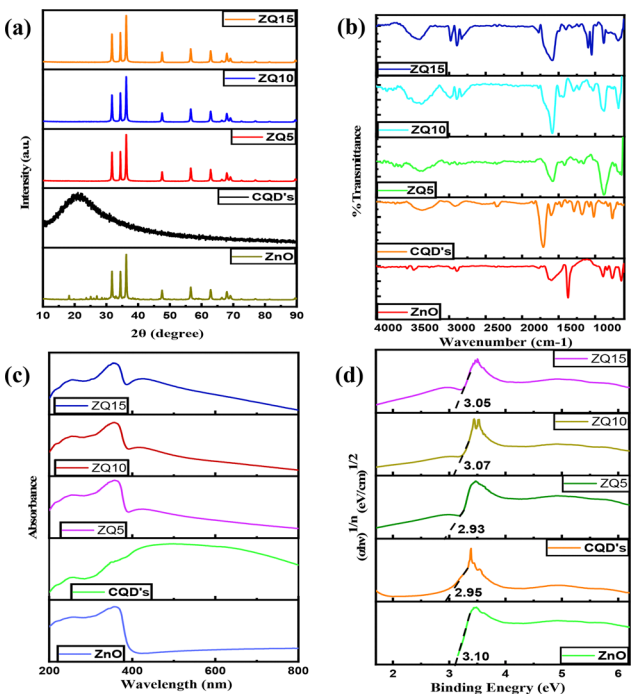

Fig. 2 (a) XRD spectra, (b) FTIR spectra, (c) UV-vis DRS spectra, and (d) Tauc's plot for ZnO, CQDs, ZQ5, ZQ10, and ZQ15.

and carboxyl groups. An absorption band at 1588 cm^{-1} was assigned to N–H bending, supported by a minor peak at 2351 cm^{-1}, which further suggested the presence of amine-related functionalities. The C–O stretching vibration was observed at 1167 cm^{-1}, confirming the oxygenated surface nature of CQDs.[29] The FTIR spectra of the nanocomposites (ZQ5, ZQ10, and ZQ15) retained the key functional group signatures of both ZnO and CQDs, though slight shifts in peak positions were observed. These spectral changes imply successful surface interactions between ZnO and CQDs, confirming the formation of a hybrid composite without disrupting the core structure of either component.

3.1.4. UV-visible DRS. The optical absorption properties of the materials were investigated using UV-vis diffuse reflectance spectroscopy (UV-DRS) to evaluate their ability to harness solar energy, an essential factor for photocatalytic activity. As presented in Fig. 2(c), ZnO exhibited strong absorption in the ultraviolet region (250–400 nm), with a sharp cut-off indicating its wide band gap nature. In contrast, CQDs displayed broader absorption features extending into the visible range.

Upon compositing, ZQ5, ZQ10, and ZQ15 hybrids demonstrated a noticeable enhancement in visible light absorption compared to bare ZnO. This red-shift in absorption is attributed to the sensitizing role of CQDs, which improve the photon capture capability of the system and extend its optical response beyond the UV region. Additionally, a visible change in material color—from white for pure ZnO to a progressively darker shade in the composites—further supports the successful integration of CQDs and the corresponding increase in visible-light harvesting capacity.

To determine the optical band gap, Tauc's relation was used as follows:

$$(\alpha h\nu)^{1/n} = A(h\nu - E_g) \quad (1)$$

In the above expression, $h\nu$ represents the energy of the incident photon, α denotes the absorption coefficient, A is a proportionality constant, and n is equal to 1/2 for direct electronic transitions. The Tauc plots of $(\alpha h\nu)^{1/2}$ *versus* $h\nu$, shown in Fig. 2(d), allowed the estimation of band gap energies for the synthesized samples. The determined E_g (optical band) values were 3.10 eV for ZnO, 2.95 eV for CQDs, 2.93 eV for ZQ5, 3.07 eV for ZQ10, and 3.05 eV for ZQ15. The slight narrowing of the band gap in the composites highlights the role of CQDs in enhancing the optical absorption and tuning the electronic properties of ZnO toward improved visible-light-driven photocatalysis.

3.1.5. Photoluminescence (PL) analysis. Photoluminescence (PL) spectroscopy was utilized to examine the recombination behavior of photogenerated electron–hole pairs in both the pristine materials and the nanocomposites. The PL spectra of ZnO, CQDs, ZQ5, ZQ10, and ZQ15 were recorded at an excitation wavelength of 325 nm, as shown in Fig. S1. A high PL intensity typically reflects rapid charge carrier recombination, which adversely affects photocatalytic efficiency, whereas a lower PL intensity suggests improved charge separation and longer carrier lifetimes. ZnO exhibited the highest PL intensity, indicating a significant rate of electron–hole recombination. CQDs also showed emission in the same region but with comparatively lower intensity. Upon the incorporation of CQDs into ZnO, a marked reduction in PL intensity was observed for all nanocomposites, confirming the role of CQDs in suppressing charge recombination. Among the composites, ZQ5 displayed the lowest PL intensity, implying the most efficient electron–hole separation and interfacial charge transfer. In contrast, ZQ10 and ZQ15 exhibited slightly higher intensities, indicating that excessive CQD loading may reduce the interfacial contact or introduce recombination centres. The trend suggests that a 5% CQD loading in ZQ5 provides an optimal balance between light absorption, electron transport, and heterojunction formation. The reduced PL intensities confirm the enhanced separation and migration of photogenerated charge carriers in the composites, contributing to their superior photocatalytic activity under solar irradiation.

3.1.6. Field emission scanning electron microscopy. Field emission scanning electron microscopy (FE-SEM) was utilized to examine the surface morphology of both the bare samples and the composites, with representative images presented in Fig. 3(a)–(c). ZnO revealed a well-defined nanoflower-like morphology,[28] offering a high surface area favourable for photocatalysis. Although the CQDs are expected to possess a spherical morphology, their nanoscale dimensions made them difficult to distinguish clearly in FE-SEM images. Consequently, HR-TEM was used for further visualization. In the ZQ5 composite, the CQDs were visibly anchored onto the surface of the ZnO nanoflowers, indicating the successful formation of the ZnO/CQD heterojunction. This architecture promotes multiple active sites and facilitates efficient light absorption and charge separation, enhancing photocatalytic degradation performance. The ZQ5 composite was subjected to elemental analysis through energy-dispersive X-ray spectroscopy (EDS), as illustrated in Fig. 3(i). The results confirmed the presence of Zn, O, C, and N (as an impurity) elements in the sample, verifying the coexistence of ZnO and CQDs in the composite. Additionally, elemental mapping images (Fig. 3(d)–(g)) demonstrated the uniform distribution of all constituent elements across the composite surface. This homogeneity is crucial for consistent charge transport and reactivity, supporting the superior photocatalytic activity observed in ZQ5.

3.1.7. High-resolution transmission electron microscopy. High-resolution transmission electron microscopy (HR-TEM) was utilized to gain deeper insight into the nanoscale morphology and lattice structure of the ZQ5 nanocomposite. As shown in Fig. 3(h) and (j), the CQDs appear well-dispersed on the surface of the ZnO nanoflowers, further confirming the formation of a well-integrated heterojunction. The layered interface and intimate contact between CQDs and ZnO are visible, supporting the effective coupling between the two components. The interplanar spacing (d-spacing) values obtained from the HR-TEM images correspond well with the diffraction planes observed in the XRD analysis, including the (002), (101), and (102) planes. These spacing values confirm the crystalline integrity of ZnO and the structural presence of CQDs in the

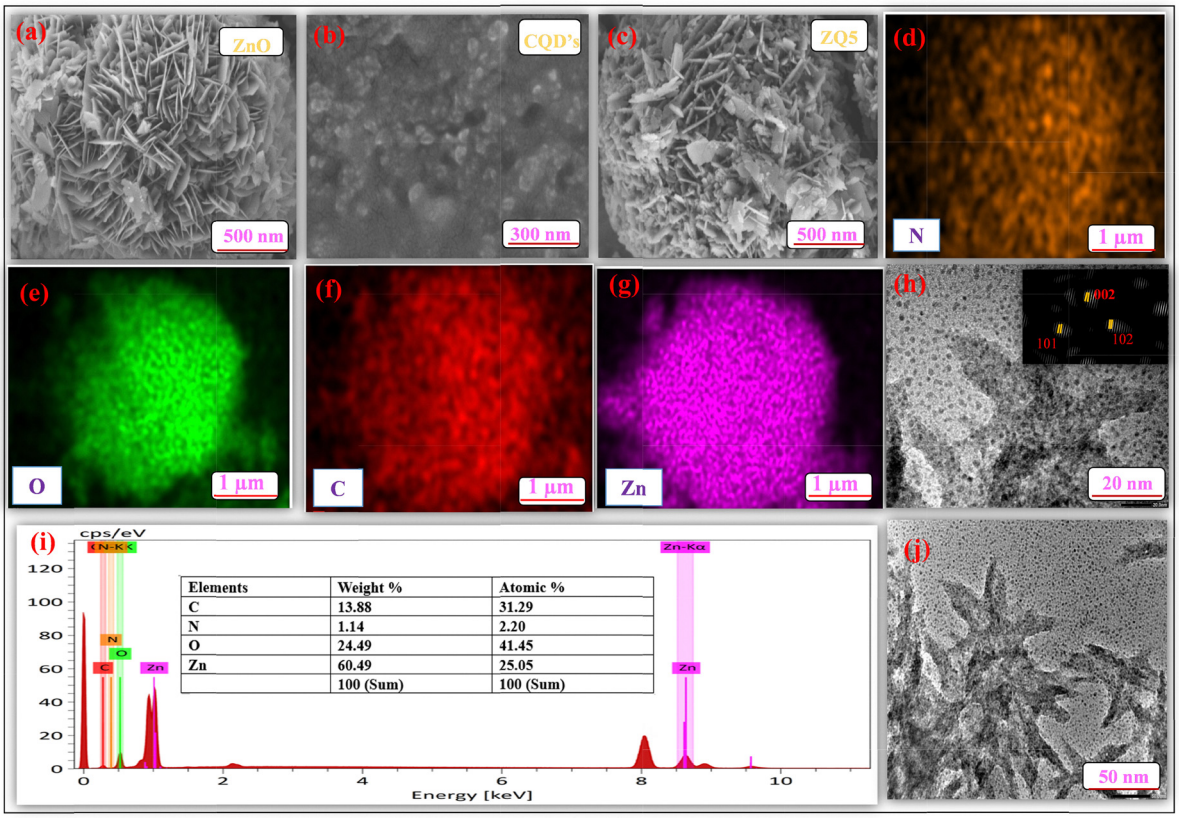

Fig. 3 FE-SEM images of (a) ZnO, (b) CQDs, and (c) ZQ5; (d)–(g) color mapping of various elements; (h) and (j) HR-TEM images of ZQ5 at different magnifications, and (i) EDS analysis of ZQ5.

composite, thereby reinforcing the conclusions drawn from the XRD data.

3.1.8. Surface properties. The textural properties of the generated nanocomposites were assessed by measuring their specific surface area. Fig. 4(a) displays the nitrogen adsorption–desorption isotherms, which clearly show type IV Langmuir behavior and H1 hysteresis loops. These loops are present in both the composite materials and their individual constituents,

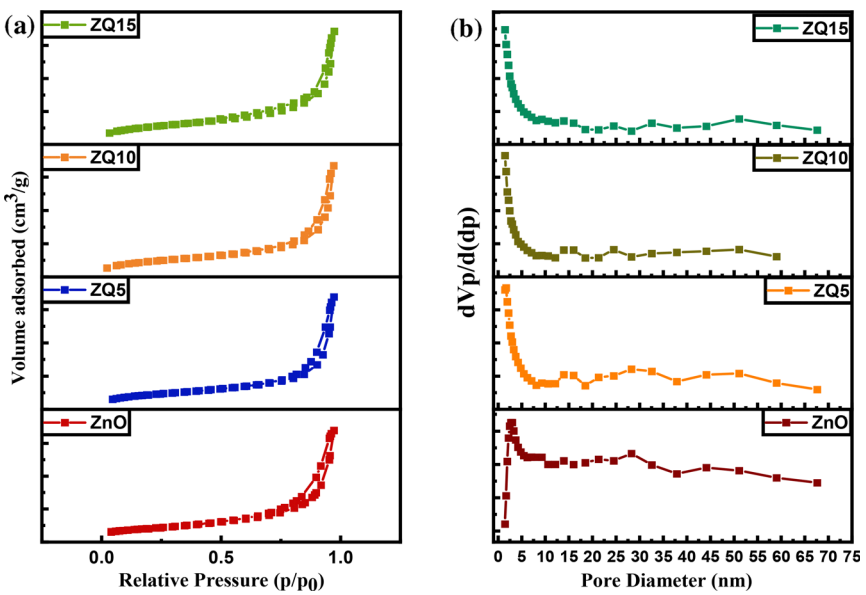

Fig. 4 (a) BET and (b) BJH plots of ZnO, ZQ5, ZQ10, and ZQ15.

indicating mesoporous structures with well-organized pore networks. As shown in Fig. 4(b), the Barrett–Joyner–Halenda (BJH) plots were used to determine the pore size distribution of ZnO, ZQ5, ZQ10, and ZQ15. A comparison of the surface area and pore volume is given in Table 1. The average pore size of ZQ5 among the other nanocomposites has the highest value, which shows maximum photocatalytic degradation. Among the composites, ZQ5 exhibits the highest photocatalytic performance. Although the incorporation of CQDs may partially block some active sites, it simultaneously enhances the overall adsorption capacity of the material and facilitates charge transfer, thereby providing a higher density of accessible reactive sites for catalytic reactions. This synergistic effect explains the superior photocatalytic activity of ZQ5 compared to the other composites.[32]

3.2. Photocatalytic activity

By tracking the methylene blue (MB) degradation under natural sunlight in Patiala, India, which has a subtropical climate, the ZQ5 nanocomposite's photocatalytic effectiveness was assessed (Thapar Institute of Engineering & Technology). The average sun irradiation during the experiments was measured using a LICOR pyranometer to be 850 W m^{-2}. For comparative light source studies, visible-light irradiation from a 45 W compact fluorescent lamp (Philips) was used and UV light exposure was achieved using a 100 W mercury lamp.

Photocatalytic experiments were conducted using a 10 mL aqueous solution of MB (10 ppm), where the catalyst dosage was maintained at 0.1 g L^{-1}. To achieve adsorption–desorption equilibrium, the suspensions were stirred for 60 minutes in the dark before irradiation. The degradation process was then initiated under natural sunlight and continued for an additional 60 minutes. Absorbance measurements were taken at regular intervals using a UV-vis spectrophotometer, with the MB λ_{max} identified at 660 nm. All degradation studies were conducted in triplicate, and the results were illustrated with error bars indicating a 5% margin to ensure reproducibility.

Photocatalytic degradation efficiency was calculated using the equation:

$$\%\text{Degradation} = \frac{A_0 - A_t}{A_0} \times 100 \quad (2)$$

where A_0 denotes the initial absorbance value of MB and A_t denotes the absorbance value of MB at time t, respectively.

Among all tested photocatalysts, ZQ5 showed the highest degradation efficiency of 97.2% within 60 minutes of solar exposure (Fig. 5(a)). The kinetic behavior of the photocatalytic reaction was further analyzed using a pseudo-first-order kinetic model:

$$\ln\frac{C}{C_0} = -kt \quad (3)$$

where C_0 and C are the initial and time-dependent concentrations of MB, respectively, and k is the apparent rate constant (Fig. S2). Based on this model, ZQ5 demonstrated a significantly higher reaction rate constant of 0.047 min^{-1}, outperforming ZnO (0.015 min^{-1}), CQDs (0.0092 min^{-1}), ZQ10 (0.019 min^{-1}), ZQ15 (0.017 min^{-1}), and commercial TiO_2 (P25) (0.0082 min^{-1}). These results underscore the enhanced photocatalytic activity of the optimized ZQ5 composition.

The synergy factor (R) was determined using the following equation:

$$R = \frac{K_{ZQ}}{K_Z + K_Q} \quad (4)$$

which quantifies the synergistic interaction between ZnO and CQDs in their composites. The ZQ5 composite exhibited the highest synergy factor among all tested samples, highlighting the superior cooperative effect between ZnO and CQDs. The combination not only improved charge separation and light absorption but also led to significantly faster degradation kinetics. A comparative summary of the calculated rate constants and synergy factors is provided in Table 2.

3.2.1. Effect of light sources. Under constant experimental settings, the ZQ5 nanocomposite was tested in ultraviolet (UV), visible, and natural sunlight to assess the impact of the irradiation type on photocatalytic efficiency. As illustrated in Fig. 5(b), the degradation of methylene blue (MB) varied significantly with the light source. Under UV illumination, a degradation efficiency of 62.1% was observed, while visible light exposure resulted in a lower efficiency of 38.8%. In contrast, the highest degradation performance (89.2%) was achieved under natural sunlight irradiation. These results underscore the superior efficacy of the ZQ5 photocatalyst when operated under solar light, likely due to the broader spectral intensity and photon flux offered by natural sunlight. The enhanced activity under solar exposure confirms the suitability of ZQ5 for real-world, energy-efficient water treatment applications, where ambient sunlight can be harnessed as a sustainable and cost-effective energy source.

3.2.2. Effect of catalyst concentration. The influence of photocatalyst dosage on methylene blue (MB) degradation was systematically evaluated using the ZQ5 composite at concentrations ranging from 0.1 g L^{-1} up to 0.6 g L^{-1} under natural sunlight. As shown in Fig. 5(f), the degradation efficiency remained relatively stable across the tested concentration range, with no significant enhancement observed beyond the lowest dosage. Within 60 minutes, the ZQ5 photocatalyst demonstrated an amazing 97% degradation of MB at a concentration of 0.1 g L^{-1}. Increasing the catalyst concentration did not yield further improvement in performance, likely due to the saturation of active sites or increased light scattering at higher dosages, which can hinder effective photon penetration. Based

Table 1 Surface properties of the synthesized photocatalysts

Catalyst	Surface area (m^2 g^{-1})	Average pore size (nm)	Total pore volume (cm^3 g^{-1})
ZnO	12.469	14.303	0.044
ZQ5	11.353	12.689	0.036
ZQ10	8.9343	12.031	0.0269
ZQ15	14.582	10.761	0.0369

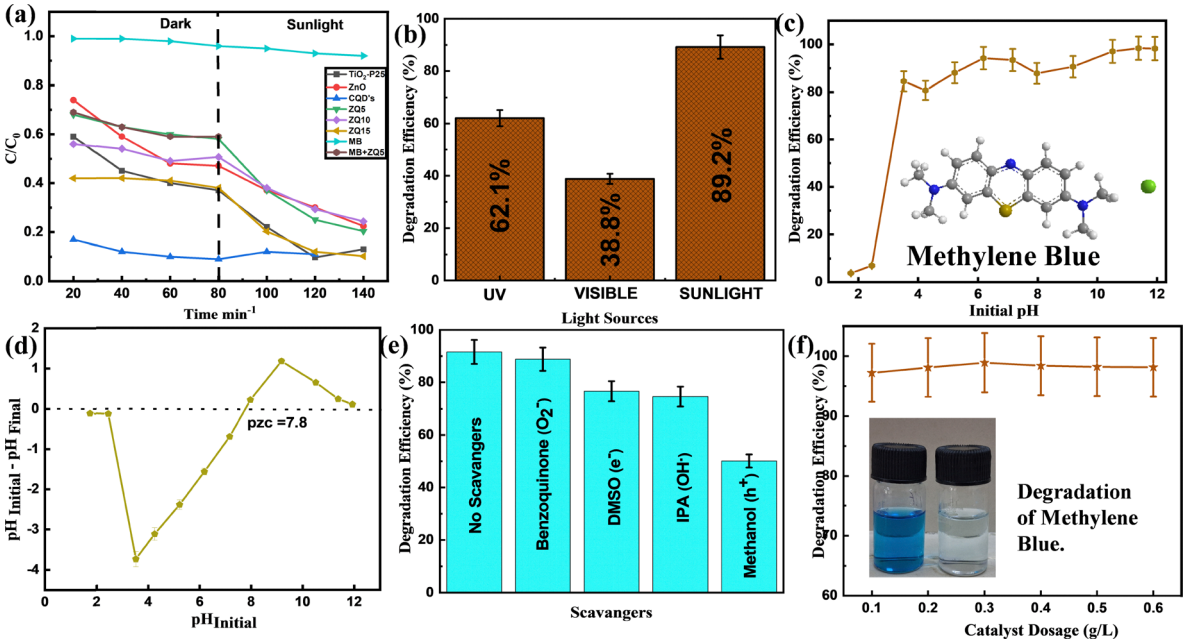

Fig. 5 (a) Degradation kinetics of MB, (b) changes in MB degradation due to different types of light sources, (c) the effect of pH, (d) the pzc of ZQ5, (e) the effect of scavengers, and (f) the effect of catalytic dose.

Table 2 Synergy factors and rate constants (k) for MB degradation

Material	Rate constant (min^{-1})	Synergy factor (R)
TiO_2–P25	0.0082	—
ZnO	0.015	—
CQDs	0.0092	—
ZQ5	0.047	2.02
ZQ10	0.019	0.81
ZQ15	0.017	0.73

on these findings, 0.1 g L^{-1} was identified as the optimal dosage and employed in all subsequent photocatalytic experiments.

3.2.3. Effect of solution pH. The pH of the dye solution is essential to determine photocatalytic performance, since it affects both the surface charge of the catalyst and the ionization state of the dye molecules.[33] Fig. 5(c) shows that the degradation efficiency of methylene blue (MB) improved markedly as the pH increased from acidic to alkaline conditions, achieving over 95% removal efficiency in the pH range of 8–12. This enhancement is primarily attributed to the surface charge behavior of the photocatalyst, governed by its point of zero charge (pzc), determined to be 7.8 (Fig. 5(d)). At pH values above the pzc, the ZQ5 surface acquires a net negative charge, which promotes electrostatic attraction toward the positively charged MB dye molecules. This enhanced adsorption facilitates more efficient charge transfer and accelerates the generation of reactive oxygen species, particularly hydroxyl radicals ($^{\bullet}OH$), through increased interaction with OH^- ions in the alkaline medium. Thus, under basic conditions (pH > 7.8), two key factors—improved dye adsorption due to favorable electrostatics and enhanced radical formation—synergistically contribute to the elevated photocatalytic degradation efficiency observed.

3.2.4. Scavenger effect and a potential charge transfer pathway. To elucidate the primary reactive species involved in the photocatalytic degradation of MB by the ZQ5 nanocomposite, radical scavenger experiments were conducted using specific quenching agents. These agents were employed to selectively inhibit different reactive species: isopropyl alcohol (IPA) for hydroxyl radicals ($^{\bullet}OH$), dimethyl sulfoxide (DMSO) for electrons (e^-), benzoquinone (BQ) for superoxide radicals ($O_2^{\bullet-}$), and methanol for photogenerated holes (h^+).[34] Fig. 5(e) illustrates the outcomes of the trapping trials. Without any scavenger, the ZQ5 system attained a maximum MB degradation efficiency of 97.7%. However, upon the addition of scavengers, a marked reduction in photocatalytic activity was observed, indicating a significant role of multiple reactive species in the degradation process. Methanol as a scavenger caused the most reduction in photocatalytic activity, indicating that photogenerated holes (h^+) contributor mainly to the degradation process. The impact of DMSO and IPA, although moderate, also confirmed the involvement of $^{\bullet}OH$ radicals and electrons in the degradation pathway. The reduction in activity in the presence of BQ pointed to the participation of $O_2^{\bullet-}$ radicals, which are known to react with BQ to form hydroquinone intermediates.[35] The electron-donating and hydrogen-bonding characteristics of DMSO further support its role in neutralizing hydroxyl radicals and mediating electron transfer.[36] Taken together, these findings confirm that holes (h^+) are the primary oxidative species, while superoxide and hydroxyl radicals, along with photogenerated electrons, also contribute to the photocatalytic breakdown of MB. The interplay between these species facilitates efficient dye degradation through both oxidative and reductive pathways, highlighting the strong photocatalytic potential of the ZQ5 heterostructure (Scheme 2).

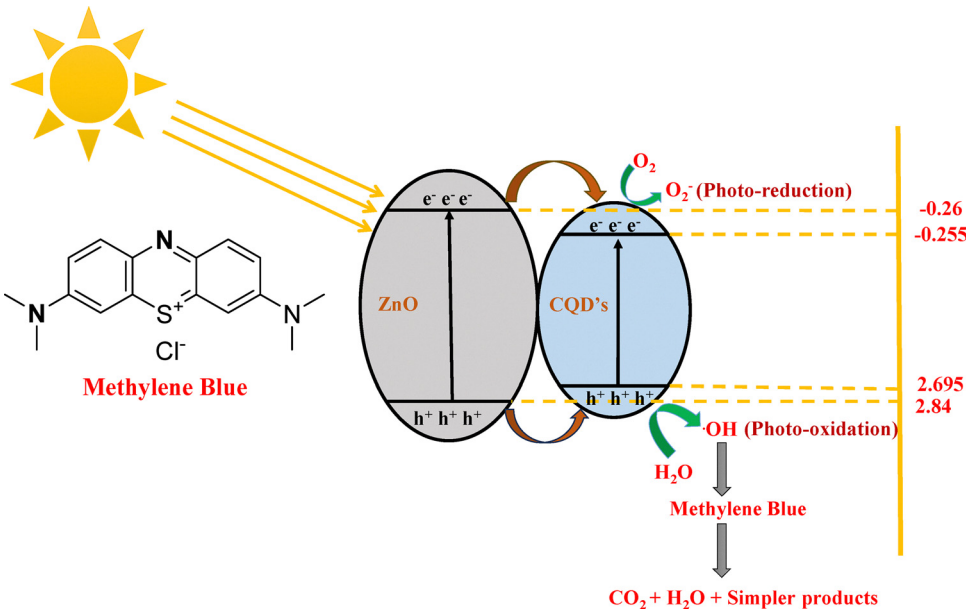

Scheme 2 Proposed mechanism for the photocatalytic degradation of MB.

$$\mathrm{ZnO/CQD} + h\nu \rightarrow \mathrm{e^-} + \mathrm{h^+} \quad (5)$$

$$\mathrm{e^-_{CB}} + \mathrm{O_2} \rightarrow \mathrm{O_2^{\bullet -}} \quad (6)$$

$$\mathrm{O_2^{\bullet -}} + \mathrm{H_2O} \rightarrow \mathrm{OH^\bullet} + \mathrm{HOO^\bullet} \quad (7)$$

$$\mathrm{h^+_{VB}} + \mathrm{OH^-} \rightarrow \mathrm{OH^\bullet} \quad (8)$$

$$\mathrm{OH^\bullet/h^+} + \text{pollutant} \rightarrow \text{degraded products} \quad (9)$$

3.2.5. Reusability studies. Beyond its catalytic activity, assessing the durability of a photocatalyst is essential for real-world applications. To evaluate the repeatability and photostability of the ZQ5 photocatalyst, multiple recycling experiments were conducted. These tests focused on examining the photodegradation of MB under identical experimental conditions, with the catalyst undergoing repeated cycles of photochemical reactions. After each cycle, the catalyst was recovered through centrifugation, thoroughly washed, and dried before being reused. As illustrated in Fig. 6(a), the degradation efficiency remained at 85% even after six consecutive cycles, indicating that ZQ5 is a reusable catalyst. The observed decline in efficiency from 97.7% to 85% could be attributed to the inevitable loss of the catalyst during the recovery process. Additionally, some residual intermediates adhered to the catalyst's surface over successive cycles, potentially blocking active sites and reducing performance. To further assess its structural stability, the ZQ5 sample was analyzed using XRD after six cycles (Fig. 6(c)). The XRD pattern confirmed that the crystal structure remained intact, with no significant shifts in the positions or intensities of the diffraction peaks, nor the appearance of any new peaks. Furthermore, FE-SEM analysis (Fig. 6(d)) verified that the composite's morphology remained unchanged throughout the degradation process.

The findings underscore the impressive stability and regenerative capability of the ZQ5 nanocomposite, positioning it as a highly promising photocatalyst for a range of photocatalytic applications moving forward.

3.2.6. Mineralization studies. The mineralization capability of ZQ5 was assessed using titrimetric methods to quantify TOC and COD. The respective values were calculated using eqn (10) and (11), with pure water serving as the reference standard.

$$\%\mathrm{TOC} = \frac{\mathrm{TOC_i} - \mathrm{TOC_f}}{\mathrm{TOC_i}} \times 100 \quad (10)$$

$$\%\mathrm{COD} = \frac{\mathrm{COD_i} - \mathrm{COD_f}}{\mathrm{COD_i}} \times 100 \quad (11)$$

In these analyses, $\mathrm{COD_i}$ and $\mathrm{COD_f}$ refer to the initial and final COD values, while $\mathrm{TOC_i}$ and $\mathrm{TOC_f}$ represent the corresponding TOC readings. Initially, the high values of TOC and COD indicated that the pollutant MB was rich in organic constituents. After 60 minutes of solar irradiation, MB showed a TOC reduction of 65% and a COD decrease of 58%. The relatively modest decrease in TOC, even with significant degradation observed, can be explained by the generation of intermediate organic compounds throughout the degradation process.[37] These intermediates are essential in the complete conversion of MB into $\mathrm{CO_2}$ and simpler products. Due to ethical constraints, real pharmaceutical or medical wastewater samples could not be used in this study. Nevertheless, as shown in Fig. 6(b), the test solutions approached near-complete mineralization, and the remaining intermediates demonstrated limited potential for further mineralization.

3.2.7. Comparison of photocatalysts. Table 3 presents a comparison of the degradation performance of the synthesized ZQ5 with other MB-removing photocatalysts reported in the

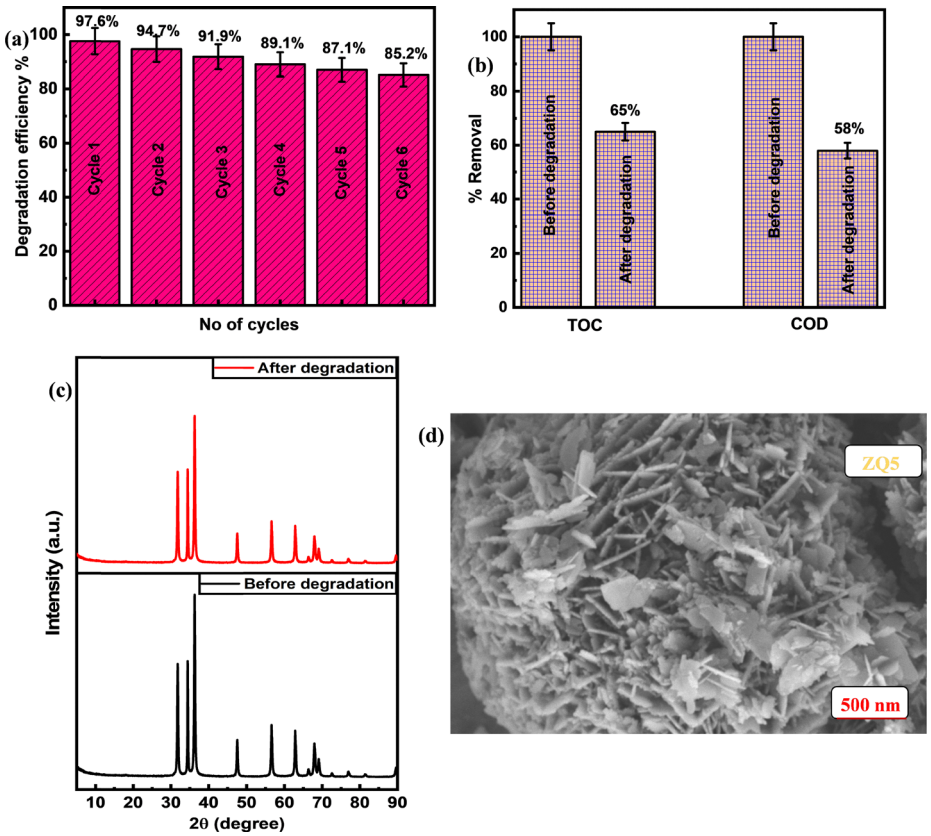

Fig. 6 (a) Reusability graph, (b) analysis of TOC and COD levels before and after degradation, (c) XRD spectra of the ZQ5 nanocomposite before and after degradation, and (d) FE-SEM image of the ZQ5 nanocomposite after degradation.

Table 3 Comparative analysis of several photocatalysts for MB photocatalytic degradation

Catalyst	Concentration of MB in ppm	Catalyst concentration in g L^{-1}	Reaction time in min	Light source	Degradation efficiency (%)	Ref.
ZnS/CdS	10	0.1	360	Visible light	73	38
WO_3/TiO_2	10	0.5	120	Visible light	27	39
$BiVO_4$/EDTA	5	1	300	Sunlight	90.88	40
(Yb,N)-TiO_2	10	3	300	Visible light	93.55	41
TiO_2/polyaniline	10	2.5	200	UV light	73	42
ZnO/CQD	10	0.1	60	Sunlight	97.7	Present work

literature. The ZQ5 nanocomposite exhibits superior photocatalytic performance to previously reported systems, achieving high degradation efficiency at lower catalyst dosages. This underscores its potential as a highly effective and scalable photocatalyst for environmental applications.

3.2.8. LC-MS. The LC-MS study revealed several mechanisms through which MB degradation occurs (Fig. S3). Before full mineralization occurs, MB (m/z = 284) undergoes hydroxylation and demethylation in pathway 1, creating intermediates at m/z = 318, 340, and 396 that further fragment into smaller pieces like m/z = 109 and 130.[43] Driven by hydroxyl radicals that encourage ring opening and molecular cleavage, pathway 2 uses hydrodynamic cavitation to create polyhydroxylated products at m/z = 350 and 366.[44] One of the two routes described in pathways 3 and 4 converts MB to m/z = 215, then to m/z = 158, and finally to m/z = 74. The other route follows m/z = 136, 137, and 109 before arriving at the same terminal product at m/z = 74, indicating complete ring destruction and demethylation.[45] These results highlight the crucial role of hydroxyl radicals in breaking down MB into less complex, safe substances (Scheme 3).

4. Conclusion

Using a hydrothermal method, a number of ZnO–CQD heterojunction photocatalysts with different molar ratios were effectively synthesized. Comprehensive characterization through XRD, FE-SEM, EDS, XPS, UV-DRS, BET, and HR-TEM confirmed the successful formation of a well-integrated heterostructure, where

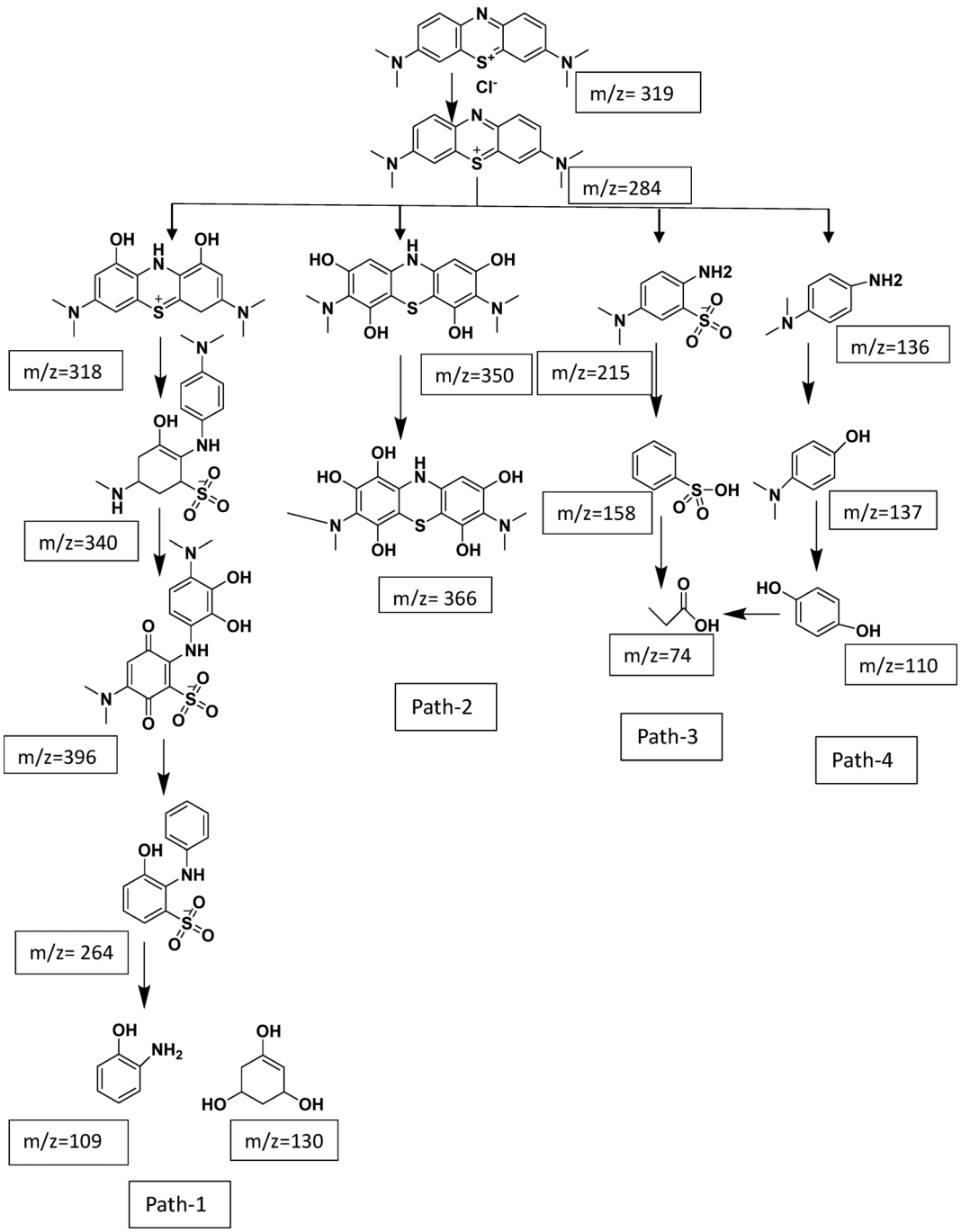

Scheme 3 Potential photocatalytic reaction route for MB degradation using the ZQ5 photocatalyst.

smaller CQDs were effectively deposited on larger ZnO nanoflowers. The photocatalytic activities of the synthesized samples were evaluated under natural sunlight using MB as a model pollutant. Among the composites, ZQ5 exhibited the most outstanding photocatalytic activity, with an apparent first-order rate constant (pseudo-first-order rate constant) of 0.047 min^{-1}, which was 5.7 times higher than that of TiO_2–P25 (0.0082 min^{-1}), 3.1 times higher than that of ZnO (0.015 min^{-1}), 5.1 times higher than that of CQDs (0.0092 min^{-1}), 2.5 times higher than that of ZQ10 (0.019 min^{-1}), and 2.8 times higher than that of ZQ15 (0.017 min^{-1}). This remarkable enhancement is primarily attributed to the composite's improved charge separation, reduced recombination rate, and suitable band gap, as evidenced by PL, BET, and UV-DRS studies. Additional investigations—including catalyst dosage, pH influence, light source variation, scavenger analysis, and reusability—demonstrated the composite's robustness under varied conditions. Trapping experiments further confirmed that superoxide radicals (O_2^-) and electrons (e^-) were the main active species responsible for MB degradation. The ZQ5 catalyst also exhibited excellent reusability, maintaining high

photocatalytic efficiency over six consecutive cycles. Post-degradation XRD and FE-SEM analyses confirmed structural stability, with no significant changes in crystallinity or morphology. The degradation mechanism was further elucidated by LC-MS analysis, which identified intermediate products, validating successful mineralization of the dye. In addition, the ZQ5 photocatalyst demonstrated superior removal efficiencies of COD (58%) and TOC (65%) when compared to conventional physicochemical methods, emphasizing its practical potential in wastewater treatment. In summary, the ZQ5 nanocomposite stands out as a highly effective, reusable, and eco-friendly photocatalyst for solar-driven degradation of organic pollutants.

Author contributions

Hitesh Bansal designed and performed the experiments, analyzed the data, and co-wrote the paper; Palkaran Sethi supervised the research, designed the experiments, and co-wrote the paper; Soumen Basu supervised the research, designed the experiments, and co-wrote the paper.

Conflicts of interest

The authors declare no conflicts of interest regarding the conduct of this study and the publication of its results.

Data availability

The data supporting the findings of this study, including characterization results, degradation kinetics, and LC-MS data, are available within the article as well as the SI file provided with this article. Supplementary information: characterization of the synthesized materials, kinetics plots, and LC-MS data. See DOI: https://doi.org/10.1039/d5ma00804b.

Acknowledgements

We are grateful to DCBC and DPMS, TIET for providing us with characterization facilities. We are also thankful to the Department of Chemical Engineering for providing access to their UV-visible spectrophotometer facilities. We are also grateful to the Department of Science and Technology (DST), Government of India, for the financial support under the FIST program, which facilitated the FTIR analysis in this study. We are also grateful to the SAIF and CIL, Punjab University for providing us with LC/MS and HR-TEM characterization facilities and to IIC, IIT Roorkee, for XPS characterization.

References

1 S. Dong, J. Feng, M. Fan, Y. Pi, L. Hu, M. Liu, J. Sun and C. Du, Recent developments in heterogeneous photocatalytic water treatment using visible light-responsive photocatalysts: a review, *RSC Adv.*, 2015, **5**, 14610–14630, DOI: 10.1039/C4RA13734E.

2 H. Deng, J. Yin, J. Ma, J. Zhou, L. Zhang, L. Gao and T. Jiao, Exploring the enhanced catalytic performance on nitro dyes via a novel template of flake-network Ni–Ti LDH/GO in-situ deposited with Ag_3PO_4 NPs, *Appl. Surf. Sci.*, 2020, **543**, 148821, DOI: 10.1016/j.apsusc.2020.148821.

3 J. Qu and M. Fan, The Current State of Water Quality and Technology Development for Water Pollution Control in China, *Crit. Rev. Environ. Sci. Technol.*, 2010, **40**, 519–560, DOI: 10.1080/10643380802451953.

4 I. Khan, I. Khan, M. Usman, M. Imran and K. Saeed, Nanoclay-mediated photocatalytic activity enhancement of copper oxide nanoparticles for enhanced methyl orange photodegradation, *J. Mater. Sci.: Mater. Electron.*, 2020, **31**, 8971–8985, DOI: 10.1007/s10854-020-03431-6.

5 A. P. Bhat and P. R. Gogate, Degradation of nitrogen-containing hazardous compounds using advanced oxidation processes: a review on aliphatic and aromatic amines, dyes, and pesticides, *J. Hazard. Mater.*, 2021, **403**, 123657, DOI: 10.1016/j.jhazmat.2020.123657.

6 R. Javaid and U. Qazi, Catalytic Oxidation Process for the Degradation of Synthetic Dyes: An Overview, *Int. J. Environ. Res. Public Health*, 2019, **16**, 2066, DOI: 10.3390/ijerph16112066.

7 A. Houas, H. Lachheb, M. Ksibi, E. Elaloui, C. Guillard and J.-M. Herrmann, Photocatalytic degradation pathway of methylene blue in water, *Appl. Catal., B*, 2001, **31**, 145–157, DOI: 10.1016/S0926-3373(00)00276-9.

8 P. Zhang, M. Xiang, H. Liu, C. Yang and S. Deng, Novel Two-Dimensional Magnetic Titanium Carbide for Methylene Blue Removal over a Wide pH Range: Insight into Removal Performance and Mechanism, *ACS Appl. Mater. Interfaces*, 2019, **11**, 24027–24036, DOI: 10.1021/acsami.9b04222.

9 C. Hou, B. Hu and J. Zhu, Photocatalytic degradation of methylene blue over TiO_2 pretreated with varying concentrations of NaOH, *Catalysts*, 2018, **8**, 575.

10 P. Sethi, S. Barman and S. Basu, Strategic tuning of GO ratios in CuBTC-GO nanocomposites for next-generation tetracycline adsorption: a deep dive into isotherms, kinetics, and thermodynamics, *Sep. Purif. Technol.*, 2025, **361**, 131311, DOI: 10.1016/j.seppur.2024.131311.

11 P. Sethi, S. Basu and S. Barman, Innovative CuBTC/g-C_3N_4 materials for tetracycline mitigation: adsorption, photocatalysis, and mechanistic perspectives, *New J. Chem.*, 2025, **49**, 8454–8471, DOI: 10.1039/D5NJ00556F.

12 M. Basibuyuk and C. F. Forster, An examination of the adsorption characteristics of a basic dye (Maxilon Red BL-N) on to live activated sludge system, *Process Biochem.*, 2003, **38**, 1311–1316, DOI: 10.1016/S0032-9592(02)00327-8.

13 G. Zhu, H. Fang, Y. Xiao and A. Hursthouse, The Application of Fluorescence Spectroscopy for the Investigation of Dye Degradation by Chemical Oxidation, *J. Fluoresc.*, 2020, **30**, 1271–1279, DOI: 10.1007/s10895-020-02591-2.

14 E. Alventosa-deLara, S. Barredo-Damas, M. I. Alcaina-Miranda and M. I. Iborra-Clar, Ultrafiltration technology with a ceramic membrane for reactive dye removal: optimization of membrane performance, *J. Hazard. Mater.*, 2012, **209–210**, 492–500, DOI: 10.1016/j.jhazmat.2012.01.065.

15 M. M. Russell, D. M. Kempisty, S. R. Kanel, S. Kurwadkar, S. W. Brittle, I. Sizemore and L. Yaal, Destruction of Aqueous Phase Organic Pollutants Using Ultraviolet Light-Emitting Diodes and Photocatalysis, *Water, Air, Soil Pollut.*, 2018, **229**, 139, DOI: 10.1007/s11270-018-3785-2.

16 Y. Zhang, M. Zhao, J. Huang, N. Zhao and H. Yu, Controllable Synthesis, Photocatalytic Property, and Mechanism of a Novel POM-Based Direct Z-Scheme Nano-Heterojunction α-Fe_2O_3/P2Mo18, *Molecules*, 2023, **28**, 6671, DOI: 10.3390/molecules28186671.

17 M. N. Chong, B. Jin, C. W. K. Chow and C. Saint, Recent developments in photocatalytic water treatment technology: a review, *Water Res.*, 2010, **44**, 2997–3027, DOI: 10.1016/j.watres.2010.02.039.

18 L. Kong, Y. Liu, L. Dong, L. Zhang, L. Qiao, W. Wang and H. You, Enhanced red luminescence in $CaAl_{12}O_{19}$: Mn^{4+} via doping Ga^{3+} for plant growth lighting, *Dalton Trans.*, 2020, **49**, 1947–1954, DOI: 10.1039/C9DT04086B.

19 C. Y. Teh, T. Y. Wu and J. C. Juan, An application of ultrasound technology in synthesis of titania-based photocatalyst for degrading pollutant, *Chem. Eng. J.*, 2017, **317**, 586–612, DOI: 10.1016/j.cej.2017.01.001.

20 T. Hisatomi, J. Kubota and K. Domen, ChemInform Abstract: Recent Advances in Semiconductors for Photocatalytic and Photoelectrochemical Water Splitting, *Chem. Soc. Rev.*, 2014, **43**, 7520–7535, DOI: 10.1039/c3cs60378d.

21 N. Roy and A. Roy, Zinc vacancy mediated structural phase transition and photoluminescence in nanocrystalline ZnS thin films, *J. Mater. Sci.: Mater. Electron.*, 2014, **25**, 1275–1279, DOI: 10.1007/s10854-014-1721-9.

22 J.-J. Xu, Y.-N. Lu, F.-F. Tao, P.-F. Liang and P.-A. Zhang, ZnO Nanoparticles Modified by Carbon Quantum Dots for the Photocatalytic Removal of Synthetic Pigment Pollutants, *ACS Omega*, 2023, **8**, 7845–7857, DOI: 10.1021/acsomega.2c07591.

23 N. Roy, A. Chowdhury and A. Roy, Observation of negative differential resistance and electrical bi-stability in chemically synthesized ZnO nanorods, *J. Appl. Phys.*, 2014, **115**, 223502, DOI: 10.1063/1.4882017.

24 N. Roy and A. Roy, Growth and temperature dependent photoluminescence characteristics of ZnO tetrapods, *Ceram. Int.*, 2015, **41**, 4154–4160, DOI: 10.1016/j.ceramint.2014.11.113.

25 N. Roy, A. Chowdhury, T. Paul and A. Roy, Morphological, optical, and Raman characteristics of ZnO nanoflowers on ZnO-seeded Si substrates synthesized by chemical method, *J. Nanosci. Nanotechnol.*, 2016, **16**, 9738–9745.

26 L. K. Adams, D. Y. Lyon and P. J. J. Alvarez, Comparative ecotoxicity of nanoscale TiO_2, SiO_2, and ZnO water suspensions, *Water Res.*, 2006, **40**, 3527–3532, DOI: 10.1016/j.watres.2006.08.004.

27 S. Qu, X. Wang, L. Qipeng, X. Liu and L. Wang, A Biocompatible Fluorescent Ink Based on Water-Soluble Luminescent Carbon Nanodots, *Angew. Chem., Int. Ed.*, 2012, **51**, 12215, DOI: 10.1002/anie.201206791.

28 S. Mohan, M. Vellakkat, A. Aravind and R. U, Hydrothermal synthesis and characterization of Zinc Oxide nanoparticles of various shapes under different reaction conditions, *Nano Express*, 2020, **1**, 030028, DOI: 10.1088/2632-959X/abc813.

29 H. Shabbir, T. Tokarski, D. Ungor and M. Wojnicki, Eco Friendly Synthesis of Carbon Dot by Hydrothermal Method for Metal Ions Salt Identification, *Materials*, 2021, **14**, 7604, DOI: 10.3390/ma14247604.

30 X.-Y. Jin, W.-Y. Ying, R.-J. Che, P. Xiao, Y.-Q. Zhou, Y. Liu, M.-Y. Liu and S.-P. Chen, CQDs/ZnO composites based on waste rice noodles: preparation and photocatalytic capability, *RSC Adv.*, 2022, **12**, 23692–23703, DOI: 10.1039/D2RA03709B.

31 H. Bozetine, Q. Wang, A. Barras, M. Li, T. Hadjersi, S. Szunerits and R. Boukherroub, Green chemistry approach for the synthesis of ZnO–carbon dots nanocomposites with good photocatalytic properties under visible light, *J. Colloid Interface Sci.*, 2016, **465**, 286–294, DOI: 10.1016/j.jcis.2015.12.001.

32 A. Mehta, A. Mishra, S. Kainth and S. Basu, Carbon quantum dots/TiO_2 nanocomposite for sensing of toxic metals and photodetoxification of dyes with kill waste by waste concept, *Mater. Des.*, 2018, **155**, 485–493, DOI: 10.1016/j.matdes.2018.06.015.

33 A. Kumar, R. Kumar and G. Pandey, Synthesis, Characterization of Titania/Polyaniline/GO Nanocomposites, and Its Photocatalytic Activity Under UV-Visible Light, *Macromol. Symp.*, 2018, **379**, 1600192, DOI: 10.1002/masy.201600192.

34 A. Kundu, S. Sharma and S. Basu, Modulated BiOCl nanoplates with porous g-C_3N_4 nanosheets for photocatalytic degradation of color/colorless pollutants in natural sunlight, *J. Phys. Chem. Solids*, 2021, **154**, 110064, DOI: 10.1016/j.jpcs.2021.110064.

35 S. Singla, S. Sharma and S. Basu, MoS_2/WO_3 heterojunction with the intensified photocatalytic performance for decomposition of organic pollutants under the broad array of solar light, *J. Cleaner Prod.*, 2021, **324**, 129290, DOI: 10.1016/j.jclepro.2021.129290.

36 H. Alamgholiloo, E. Asgari, S. Nazari, A. Sheikhmohammadi, N. Noroozi Pesyan and B. Hashemzadeh, Architecture of bimetallic-MOF/silicate derived Co/NC@mSiO_2 as peroxymonosulfate activator for highly efficient ciprofloxacin degradation, *Sep. Purif. Technol.*, 2022, **300**, 121911, DOI: 10.1016/j.seppur.2022.121911.

37 S. Singla, P. Devi and S. Basu, Highly Effectual Photocatalytic Remediation of Tetracycline under the Broad Spectrum of Sunlight by Novel $BiVO_4$/Sb_2S_3 Nanocomposite, *Catalysts*, 2023, **13**, 731, DOI: 10.3390/catal13040731.

38 N. Soltani, E. Saion, M. Hussein, M. Erfani, A. Abedini, G. Bahmanrokh, M. Navasery and P. Vaziri, Visible Light-Induced Degradation of Methylene Blue in the Presence of Photocatalytic ZnS and CdS Nanoparticles, *Int. J. Mol. Sci.*, 2012, **13**, 12242–12258, DOI: 10.3390/ijms131012242.

39 L. Yang, Z. Si, D. Weng and Y. Yao, Synthesis, characterization and photocatalytic activity of porous WO_3/TiO_2 hollow microspheres, *Appl. Surf. Sci.*, 2014, **313**, 470–478, DOI: 10.1016/j.apsusc.2014.05.230.

40 W. Ma, Z. Li and W. Liu, Hydrothermal preparation of $BiVO_4$ photocatalyst with perforated hollow morphology and its performance on methylene blue degradation, *Ceram. Int.*, 2015, **41**, 4340–4347, DOI: 10.1016/j.ceramint.2014.11.123.

41 J. Zhang, L. J. Xu, Z. Q. Zhu and Q. J. Liu, Synthesis and properties of (Yb, N)-TiO_2 photocatalyst for degradation of methylene blue (MB) under visible light irradiation, *Mater. Res. Bull.*, 2015, **70**, 358–364, DOI: **10.1016/j.materresbull.2015.04.060**.

42 K. R. Reddy, K. V. Karthik, S. B. B. Prasad, S. K. Soni, H. M. Jeong and A. V. Raghu, Enhanced photocatalytic activity of nanostructured titanium dioxide/polyaniline hybrid photocatalysts, *Polyhedron*, 2016, **120**, 169–174, DOI: **10.1016/j.poly.2016.08.029**.

43 O. Intharaksa, S. Nanan, N. Patdhanagul, T. Panphojan, T. Srikakul, N. Tantisuwichwong, N. Tantisuwichwong and R. Dulyasucharit, Preparation of magnetic CuO/Fe_3O_4/ZnO photocatalyst for complete degradation of methylene blue under natural sunlight irradiation, *J. Phys. Chem. Solids*, 2023, **182**, 111577, DOI: **10.1016/j.jpcs.2023.111577**.

44 Y. Cao, G. Wu, Y. Huang and C. Huang, Synergistic Degradation of Methylene Blue by Hydrodynamic Cavitation Combined with Hydrogen Peroxide/Vitamin C System, *ACS Omega*, 2024, **9**, 39997–40009, DOI: **10.1021/acsomega.4c05815**.

45 J. Lin, Z. Luo, J. Liu and P. Li, Photocatalytic degradation of methylene blue in aqueous solution by using ZnO–SnO_2 nanocomposites, *Mater. Sci. Semicond. Process.*, 2018, **87**, 24–31, DOI: **10.1016/j.mssp.2018.07.003**.